Nano Energy (2015) 15, 755–765

Available online at www.sciencedirect.com

ScienceDirect

journal homepage: www.elsevier.com/locate/nanoenergy

RAPID COMMUNICATION

Control over large-volume changes of lithium battery anodes *via* active-inactive metal alloy embedded in porous carbon

Nasir Mahmood[a], Jinghan Zhu[a], Sarish Rehman[a], Quan Li[b], Yanglong Hou[a]

[a]*Department of Materials Science and Engineering, College of Engineering, Peking University, Beijing 100871, China*
[b]*Department of Physics, The Chinese University of Hong Kong, Shatin, New Territory, Hong Kong, China*

Received 14 February 2015; received in revised form 26 May 2015; accepted 29 May 2015
Available online 6 June 2015

KEYWORDS
Lithium ion battery;
CoSn alloy;
Long cyclic life;
Large volume changes;
High capacity

Abstract
Large volume changes and limited access to redox sites of high capacity anode materials are great challenges. Although, various strategies were adopted but still results are far from required values for their practical usage. Here, we have designed a unique structure to prevent surface reaction and structural disintegration meanwhile intrinsic conductivity is improved to involve all redox sites in conversion reaction. $CoSn_x$@C–PAn hybrid was synthesized through aqueous chemical route, Co doping in tin make accessible all redox sites by faster conduction of electrons while its hard nature relaxes internal stress, carbon shell prevents surface reaction and brings well control on solid electrolyte interface (SEI) film by maintaining barrier between electrode surface and electrolyte and nitrogen doped porous carbon provides faster diffusion of Li^+ deep in electrode make possible high mass loadings and conduction highway for electrons. Furthermore, porous carbon also provides room to compensate volume expansion and keeps electrode structure stable. Because of its unique structure hybrid shows excellent reversible capacity of 2044 mAh/g (retention 100%) with mass loading of 3.8 mg/cm^2 along with long cyclic life up to 1000 cycles and bears high rate capability (20 A/g).We believe that present study makes possible the use of high capacity materials in applications.

Introduction

Presently, lithium ion batteries (LIBs) have got tremendous attention due to their high energy densities and have been considered as promising power source for future electric

E-mail address: hou@pku.edu.cn (Y. Hou).

http://dx.doi.org/10.1016/j.nanoen.2015.05.035
2211-2855/

vehicles (EV) [1–4]. Therefore, in order to achieve the practical applications of LIBs in EVs, there are numerous efforts on seeking for high performance anode materials that possess high capacity and excellent stability with long cyclic life [5-7]. Metallic tin (Sn) is considered as a potential substitute for conventional graphite anode (372 mAh/g) due to its high theoretical capacity (992 mAh/g) and thermal stability [8,9]. However, structural disintegration, larger diffusion barrier, limited access to redox sites and loss of electrical contact have long been identified as primary reasons for capacity loss and poor cyclic life of Sn-based anodes [10,11]. Although nanochemistry plays a critical role to accommodate volume strains by developing nanosized structures of Sn, their use is still limited by unstable solid electrolyte interface (SEI) layer on the surface and poor internal conductivity [8,10,12]. As the organic electrolytes decompose at the working potential of <0.5 V *vs.* Li^+/Li and forms a thin SEI layer [13,14]. But the expansion and contraction of Sn during alloying and de-alloying causes deformation and breakage of the SEI layer, respectively [11,15,16]. As a result, formation of new SEI on freshly exposed Sn surface eventually block Li^+ transport *via* accumulation within SEI and causes poor Coulombic efficiency (CE) of cell [10,17]. As a consequence, the capacity decays as SEI thickness increases while most of Sn active material remains electrically connected [12]. However, nanosized designing has improved the cyclic life with enhanced performance but simple reduction of crystallite size to nanoscale has introduced new fundamental challenges [18,19]. Large surface area exposed to electrolyte and higher surface energy that increase side reactions, results in lower CE and causes thermal runway which leads to internal short circuit due to melting of separator [20-23]. Furthermore, low tap density increases thickness of electrode at high mass loading and leads to low volumetric capacity by increasing Li^+ transfer pathway [14]. Generally, poor electrical properties are observed due to higher inter-particle resistance which is further dominated by volume changes during charging–discharging, affecting cyclic life of electrode drastically [10]. A lot of efforts have been devoted by developing electrolyte blockage layers, creating void space *via* void engineering and making their composites with elastically strong graphene and inactive hard metals to sustain the structure and improve the cyclic life of Sn-based electrodes [21,24-29]. However, to the best of our knowledge, stability concerns for long cyclic life and high performance with good CE and capacity retention (CR_t) at higher mass loadings (>3 mg/cm^2) has not been reported yet for Sn-based materials. To achieve this, a careful design of electrode materials, is highly required, that maintains faster and deep transfer of Li^+, provides better pathway for electron and ions movement, prevents surface reactions with electrolyte and keeps the structural integrity of electrode [30]. Furthermore, Han et al. also investigated theoretically that fused graphitic C_6 can deliver >2000 mAh/g *via* accumulation of Li^+ through reversible reaction Li_6/C_6 [31]. Thus, utilizing the above design with conductive network containing fused C_6 backbone can bring higher capacity.

Here, we present an architectured design to overcome the aforementioned problems associated with Sn-based electrodes to bring high performance with longevity at low cost. An active–inactive metal alloy sealed in carbon shell and embedded in nitrogen-doped porous graphitic carbon (N-PGC) matrix named as $CoSn_x$@C–PAn is developed *via in-situ* polymerization and annealing processes. This nanostructure has multiple advantages: (1) doping of electrochemically inactive Co prevents structural changes and enhances internal conductivity of Sn to involve all redox sites in conversion reaction. (2) The nanosized particles can accommodate large volume strains, hard Co improves CR_t and electrochemical active Sn brings about high capacity. (3) The mixed phase provides large grain boundary densities for enhanced interfacial Li^+ storage, channels for faster Li^+ diffusion by reducing the diffusion path below 10 nm. (4) Carbon shell completely encapsulates nanoparticles (NPs) and thus prevents surface reactions by controlling direct contact with electrolyte and limit SEI on outer side with controlled thickness. (5) The carbon framework provides faster transport highways for electrons and Li^+ *via* pore walls and pores, respectively. (6) High surface area and well-defined pore size distribution improves the active surface area of the hybrid minimizing percentage of inactive material through deep transport of electrolyte and make possible high mass loadings. (7) The existence of large nitrogen contents and graphitic ring (make possible Li_6/C_6 conversion reaction) improve the overall conductivity and electrochemical activity of hybrid to bring high performance. With such a rational design, $CoSn_x$@C–PAn hybrid shows excellent discharge capacity of 2044 mAh/g with extraordinary CE and CR_t of $\sim$100% after 100 cycles at 0.2 A/g with mass loading of 3.8 mg/cm^2. Furthermore, hybrid was tested at current density of 10 A/g for 1000 cycles to explore the stability for long cyclic life and rate capability at higher charge–discharge rates (20 A/g), interestingly, hybrid shows excellent capacity (1256 mAh/g) with high CE and CR_t ($\sim$100%) after 1000th cycle at current density of 10 A/g. It is believed that the presented design will be very helpful to overcome the large-volume changes in electrode materials for energy storage devices with much improved capacity values.

Experimental section

The synthesis of Sn, Sn@C, PAn, N-PGC and characterization part are provided in supporting information.

Synthesis of Co_2SnO_4 nanoparticles

Initially, the stoichiometric amounts of $SnCl_4 \cdot 5H_2O$ (176 mg), $CoCl_2 \cdot 6H_2O$ (238 mg) and CTAB (400 mg) are mixed in 20 mL of water and stirred with heating unless temperature reaches to 85 °C. Subsequently, 20 ml of 4 M NaOH solution was added and the mixture was stirred for 60 min at 85 °C. After the completion of reaction, the product was collected by centrifugation and washed six times with water and ethanol, repeatedly. Finally, the solid product was dried at 70 °C for 6 h in a vacuum oven.

Synthesis of Co_2SnO_4-PAn hybrid

Co_2SnO_4–PAn hybrid was synthesized *via in-situ* polymerization of aniline monomers with Co_2SnO_4 NPs. Initially 50 mg of aniline monomers was stirred for 5 min in water and pH of the solution was turned acidic using HCl. Afterward, the

50 mg of NPs was added and the reaction mixture was stirred further for 10 min. Finally, the addition of APS (114 mg) as oxidant was done and reaction mixture was stirred for 24 h. After the completion of polymerization addition of ammonia solution was carried out and stirred for further 3 h to turn the PAn salt (green) to PAn base (blue). At last, the final product was centrifuge and wash 6 times with water and ethanol repeatedly. The Final product was dried at 70 °C for 6 h under vacuum.

Synthesis of $CoSn_x$@C-PAn hybrid

$CoSn_x$@C-PAn hybrid was prepared by the thermal annealing process. Co_2SnO_4-PAn hybrid was annealed at 900 °C for 1.5 h with the heating rate of 2 °C/min under reducing atmosphere of Ar/H_2. Co_2SnO_4 NPs were also treated under the same condition to obtain $CoSn_x$ for comparative study.

Results and discussion

Scheme 1 is presenting the synthesis strategy for $CoSn_x$@C-PAn hybrid; first Co_2SnO_4 NPs were synthesized *via* wet-chemistry using co-precipitation of respective salts. Then *via in-situ* polymerization, NPs encapsulated polyaniline (PAn, green as emerladine salt) were grown in rod shape morphology which were further converted to emerladine base (blue) using NH_3 (the yield of hybrid can be easily increased or decreased by controlling the amount of aniline and NPs, without effecting electrochemical properties of hybrid). To obtain $CoSn_x$@C-PAn hybrid, the annealing process of Co_2SnO_4-PAn hybrid was performed at 900 °C for 90 min at a heating rate of 2 °C/min under reducing atmosphere, which significantly reduce Co_2SnO_4 NPs to $CoSn_x$ alloy and build an uniform carbon shell on the surface of $CoSn_x$ NPs. Furthermore, N-PGC was obtained from PAn *via* annealing, has high surface area and well-defined micropores, additionally annealing effectively removed existing oxygenated groups that cause thick SEI layer [32]. It is perceived that the nanoporous carbons obtained from the polymer *via* pyrolysis will form interconnected nanochannels and electronically conductive walls for both Li^+ and e^- transport, respectively. However, nanocrystals of Sn and Sn@C were also synthesized to explore the effect of active-inactive metal alloy and porous carbon substrate on the electrochemical properties of Sn. Furthermore, the lithium storage mechanism is also illustrated in Scheme 1, as shown in Scheme 1 that lithium can be stored through intercalation chemistry both in the carbon matrix *via* Li_x/C_6 (X=1-6) conversion reaction and can contribute capacity up to 2000 mAh/g depending on the number of lithium intercalated and at Li^+ storage at grain boundaries through space charge layer. Further, the diffusion of Li^+ becomes easier and faster through the grain boundaries inside the NPs as shown by the arrows which results faster insertion and conversion reaction. In fact the porous carbon maintain the faster diffusion outside the NPs and grain boundaries maintain faster diffusion inside the NPs as results higher rate capability achieved. Further, existence of Co inside maintain the continues flow of electron to redox sites and *vice versa* that utilizes all the redox centers to bring higher performance, its hard nature prevents the rapturing of carbon shell, as results direct contact of Sn with electrolyte is inhibited and SEI film was blocked outside the carbon coating around NPs. Further surface protection blocked the undesired side reaction to prevent the formation of lithium dendrites on surface and keep the entire structure of electrode stable.

To reveal the structure and composition of as-synthesized $CoSn_x$@C-PAn hybrid, the x-ray diffraction (XRD) analysis, x-ray photoelectron spectroscopy (XPS), scanning transmission electron microscope (STEM) and Raman spectroscopy were carried out. Figure 1a presents XRD patterns of Co_2SnO_4, Co_2SnO_4-PAn and $CoSn_x$@C-PAn, from where it is observed that Co_2SnO_4 NPs show their typical peaks well-matched with standard card JCPDS no. 29-0514. An additional peak exist at 61.4° corresponds to the (220) plane of CoO (JCPDS no.48-1719). Interestingly, broad peaks were observed after PAn grown on NPs due to its amorphous structure, as perceived from XRD analysis of pure PAn shown in Figure S1, [33] which confirms complete encapsulation of NPs without aggregation. However, after annealing treatment, regular structure of PAn was changed to porous graphitic carbon and well-defined peaks of $CoSn_x$ were observed corresponding to three phases, $CoSn_2$ (JCPDS no. 25-0256), CoSn (JCPDS no. 02-0559) and $CoSn_3$ (JCPDS no. 48-1813). Phase segregation of heterogeneous CoSn crystallites with multiple phases observed here is due to higher temperature synthesis [8,26]. It is worth noting that mixed phase has multiple advantages over pure phase likewise, high grain boundary

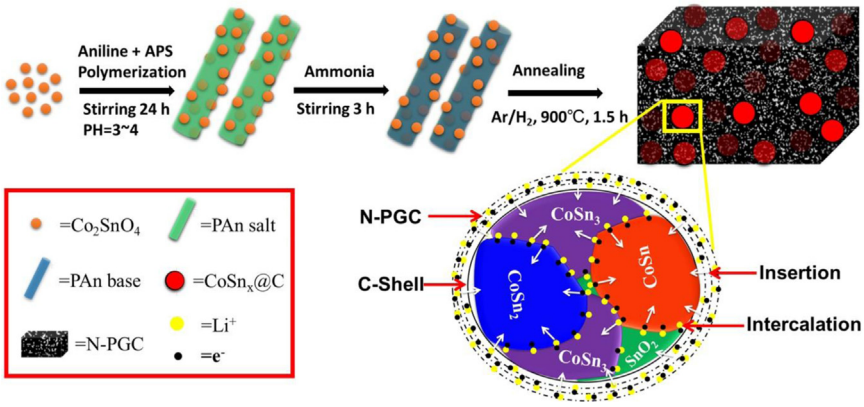

Scheme 1 Schematic illustration of synthesis method for $CoSn_x$@C-PAn *via in-situ* polymerization and annealing processes; further presenting the mechanism of lithium storage in the hybrid.

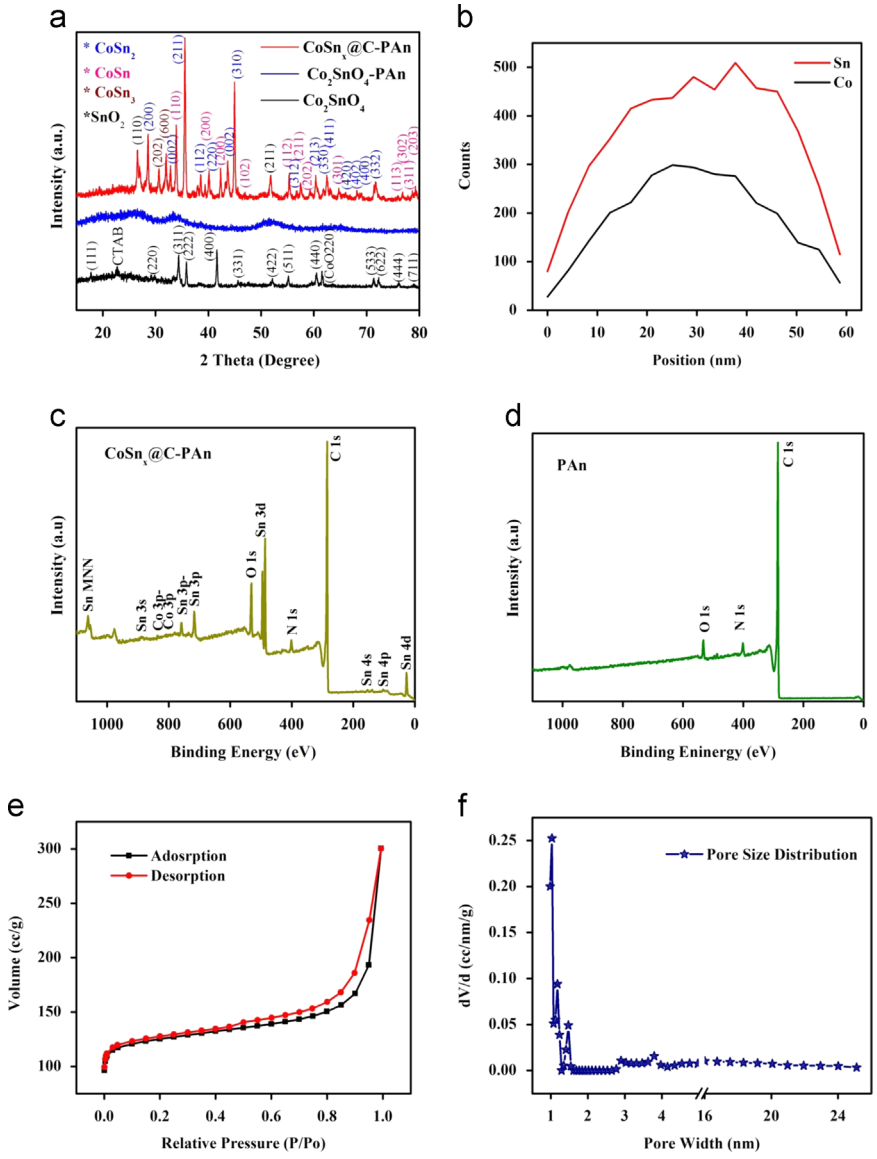

Figure 1 (a) XRD patterns of Co_2SnO_4, Co_2SnO_4-PAn and $CoSn_x$@C-PAn hybrids. (b) HAADF-STEM line profile analysis of $CoSn_x$@C-PAn hybrid. XPS spectrums of (c) $CoSn_x$@C-PAn hybrid and (d) PAn. (e) BET nitrogen adsorption-desorption isotherm of $CoSn_x$@C-PAn. (f) Pore size distribution measured using BJH adsorption.

densities enhance the interfacial Li^+ storage through space layer charge and thus offer large capacity and provide channels for faster transport of Li^+ in the NPs [34,35]. XRD pattern of $CoSn_x$@C-PAn also shows two diffraction peaks at 26.6° and 51.7°, attributed to (110) and (211) reflections of SnO_2, respectively (JCPDS no. 41-1445).

Raman spectrum of $CoSn_x$@C-PAn shows typical D- and G-bands with I_D/I_G ratio 1.09 which confirms graphitic nature of carbon matrix obtained from PAn (Figure S2), a little higher intensity of D-band is attributed to the existence of NPs [5,36]. Furthermore, XRD pattern of PAn after annealing treatment verified the graphitic nature of extracted carbon as strong broad peak near 26° (Figure S1) [6,37]. The existence of C=C, C-N, C-H and NH_2 was further confirmed by Fourier transform infrared (FTIR) spectroscopy, which emphasizes the graphitic nature of carbon with nitrogen doping (Figure S3) [33]. XRD pattern of Sn is shown in Figure S4, well-defined reflection peaks exactly matched with JCPDS no. 04-0673, delineating pure phase of Sn NPs Figure 1b and S5 show the elemental line profile and STEM image of a $CoSn_x$@C-PAn, respectively, line scan for bimetallic alloy was obtained with energy dispersive spectroscopy (EDS) in high-angle annular dark field STEM (HAADF-STEM). The elemental distribution line for Sn (red) and Co (black) confirm that the alloy has a consistent chemical composition throughout the entire NP with higher concentration of Sn. Therefore, due to homogenous distribution cobalt can easily transfer electron from carbon shell to all internal redox sites to carry on the conversion reaction and *vice versa*. Furthermore, faster transfer of electrons to redox sites and accessibility of all redox sites through Co doping improved the CR_t of the electrode even after long cyclic life. It is also expected that any strain generated by Sn volume change during lithiation and de-lithiation should

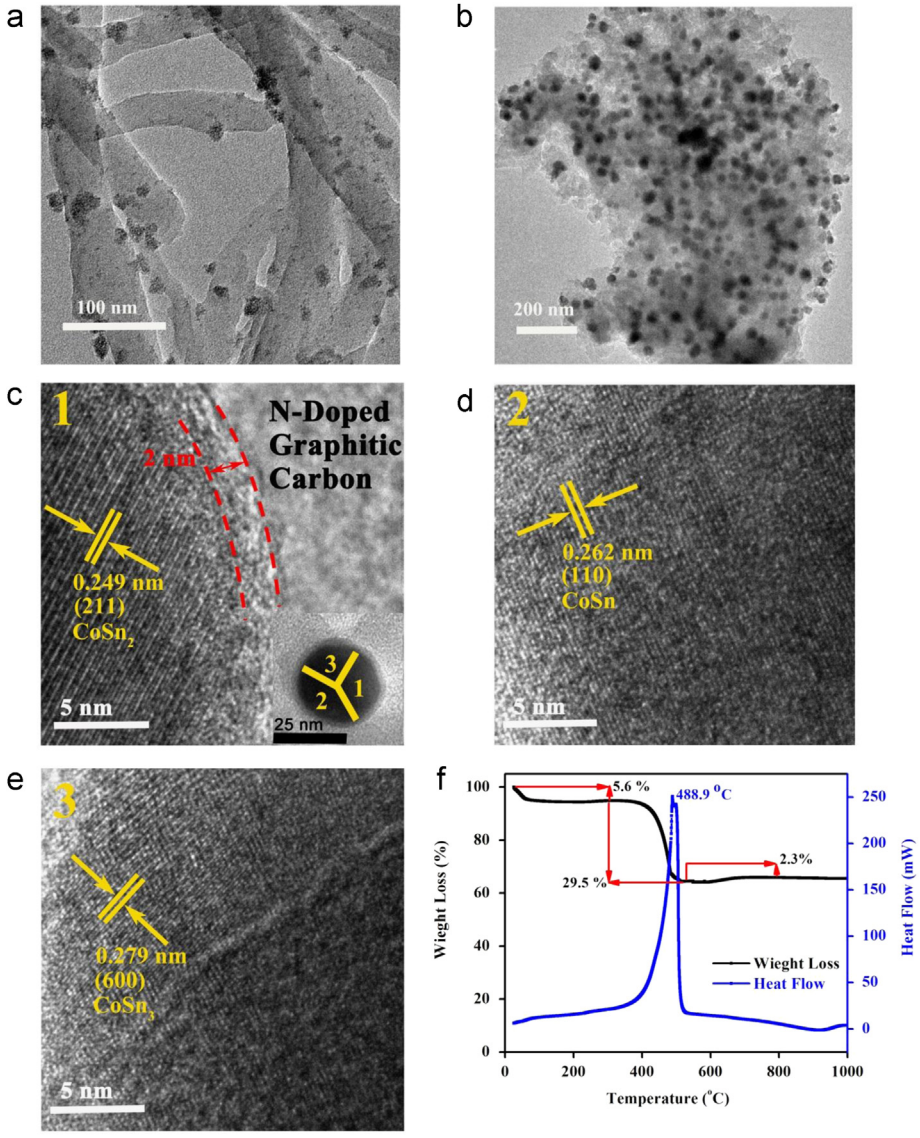

Figure 2 TEM images of (a) Co_2SnO_4-PAn hybrid and (b) $CoSn_x$@C-PAn hybrid. (c) HRTEM image of the $CoSn_x$@C-PAn hybrid at position 1 (the inset is enlarge image to show uniform carbon shell on NPs and position of HRTEM analysis), (d) HRTEM image of the $CoSn_x$@C-PAn hybrid at position 2 and (e) HRTEM image of the $CoSn_x$@C-PAn hybrid at position 3. (f) TGA/DSC curves of $CoSn_x$@C-PAn hybrid.

be evenly distributed and compensated by hard counterpart (Co). To further confirm the composition of $CoSn_x$@C-PAn hybrid, XPS studies were carried out for both hybrid and PAn (Figure 1c and d), the peaks of core levels of Co, Sn, N and C confirms the presence of all chemical species. The concentration of each element calculated from XPS is 89.76%, 6.08%, 2.50%, 1.56% and 0.10% for C, O, N, Sn and Co, respectively, as XPS is a surface detection technique thus lower metallic contents were found because of surface coverage but still the concentration of Sn is higher than Co. The presence of little higher concentration of oxygen in $CoSn_x$@C-PAn than PAn suggests that homogeneous precipitation of single phase CoSn is difficult due to existence of oxidized metallic ions instead of pure metal, in accordance with XRD results. Further, high resolution Sn3d XPS spectrum shows the existence of oxidized form of tin that is SnO_2 (Figure S6). Furthermore, the existence of large C peak in XPS results further indicate complete coverage of NPs by carbon, which is crucial for limiting the thickness of SEI layer on the outer surface of NPs *via* preventing the direct contact of NPs and electrolyte. Surface area and porosity are important factors that are beneficial in electrochemical energy storage especially batteries to improve the Li^+ diffusion [38]. However, fabrication of active nanomaterials with porous carbon substrate not only stabilizes structure of nanomaterials, but also provides electrical highway to electrons *via* walls of pores as well as faster pathway to ions through pores. Furthermore, nanoporosity results in complete wetting of C6 fused aromatic carbon matrix to fulfill the desired conversion reaction of Li_6/C_6 to bring maximum possible performance as discussed below [31,39]. In present study, PAn was converted to N-PGC by annealing process without any acid or base treatment, and high surface area of 438.5 m^2/g with well-defined pore size of ~1-1.5 nm was obtained (Figure 1d and e). Homogeneous pore size distribution with high surface area provides

efficient mass movement and larger space for Li^+ storage as well as relaxes the strains of NPs.

Transmission electron microscope (TEM) images of Co_2SnO_4-PAn and $CoSn_x$@C-PAn hybrids are presented in Figure 2. The Co_2SnO_4 NPs are well-dispersed and embedded in PAn rods without aggregation on surface (Figure 2a). Interestingly, it is found that if polymerizing reagent (ammonium persulfate, APS) was added before the addition of NPs, NPs only aggregate on the surface of PAn rods (Figure S7) [40]. In fact, addition of APS start polymerization without NPs, but earlier addition of NPs causes polymerization on the surface of NPs in presence of hydrochloric acid (HCl) which ionizes the aniline and increase its affinity towards NPs, resulting complete encapsulation of NPs and well-define morphology. It is worth noting that NPs are integrated as dimer or trimer in Co_2SnO_4-PAn hybrid as compared to individual NPs (Figure S8). These dimers and trimers fused during heat treatment, transforming into NPs with average size of 40 nm formed inside N-PGC (Figure 2b, the NPs size distribution is shown in Figure S9). The TEM image of $CoSn_x$@C-PAn reveals that NPs are evenly distributed and well embedded in N-PGC matrix. Furthermore, it is also perceived that N-PGC matrix has multidimensional structure due to random stacking of PAn rods to facilitate the faster mass transportation and enhance the wettability of the C_6 matrix. However, the presence of circular rings with bright spots in selected area electron diffraction (SAED) pattern of $CoSn_x$@C-PAn clearly depicts the existence of $CoSn_x$ alloy in hybrid (Figure S10) and is in accordance with the XRD results mentioned above. It is noted that the PAn grew in three dimensional networks (Figure S11a, mechanism is discussed in supporting information Scheme S1), which provides higher surface area to hybrid while PAn keeps its multidimensional structure even after annealing treatment at high temperature (Figure S11b). The aim of surface protection of NPs was achieved through *in-situ* polymerization of aniline monomers on the surface of NPs rather than construction of simple conduction highway for ions and electrons. It is found that during heat treatment the aniline attached on NPs surface shaped a uniform shell of carbon (the inset in Figure 2c) and additional PAn developed N-PGC. It is well-known that NPs size distribution strongly affects the electrochemical performance and tap density of nanomaterials. To obtain narrow size distribution, heat treatment at different rates (2, 5 and 10 °C/min) was carried out (Figure 2b, S12a and S12b). It is scrutinized that as heating rate was reduced from 10 to 2 °C/min, size distribution became narrower and remarkably carbon shell formed only at lower heating rate. Furthermore, longer time annealing was also adopted with aim to get rid of oxide species but it result in poor size distribution which is not suitable for better performance (Figure S13). To further confirm the structure and existence of electrolyte blockage layer, high resolution TEM (HRTEM) studies were carried out, from Figure 2c it can be seen that the surface of NP is completely covered by ~2.2 nm uniform carbon shell. Furthermore, inter-planar distance measurements make sure the existence of both electrochemically active (Sn) and inactive (Co) metals, the measured *d*-spacing of 0.249 nm at position 1 (inset of Figure 2c) corresponds to the (211) plane of $CoSn_2$ (JCPDS no. 25-0256) as shown in Figure 2c. To explore the segregation of multiphase, advantages of higher grain boundary density and interfacial Li^+ storage at grain boundaries (called buried interfaces) *via* space layer charge and brings additional capacity, the NP is characterized by HRTEM at different positions as shown in the inset of Figure 2c. The HRTEM analysis at position 2 (inset of Figure 2c) shows the inter-planar distance of 0.262 nm, which corresponds to (110) plane of CoSn phase that is in accordance with standard card (JCPDS No. 02-0559) as shown in Figure 2d. However, *d*-spacing of 0.279 nm is calculated from the HRTEM analysis of position 3 (inset of Figure 2c) which corresponds to (600) plane of $CoSn_3$ according to the standard card (JCPDS No. 48-1813) as shown in Figure 2e. Thus, HRTEM studies confirm the proposed mechanism (Scheme 1) of faster mass transfer *via* grain boundaries and larger Li^+ storage to bring higher capacity, long stable cyclic life and better rate capability. The content of the metallic constituents ($CoSn_x$) are calculated to be 65% using thermal gravimetric analysis (TGA) as carbon wipe-out at 488 °C through oxidation determined by differential scanning calorimetry (DSC, Figure 2f). An increase in weight later near 700 °C is due to the oxidation of metallic species. The TEM image of Sn NPs (Figure S14a) shows that NPs grew in the size of ~20 nm with well-defined structure confirmed through SAED (Figure S14b). A 2.2 nm thick carbon shell is also constructed on pure Sn NPs (Sn@C, Figure S14c and d) for the sake of comparative electrochemical study with $CoSn_x$@C-PAn.

The benefits of rational design of $CoSn_x$@C-PAn for Li^+ storage were investigated through electrochemical response of the obtained hybrid, by developing as anode in coin type cell. The redox response of hybrid was delineated by cyclic voltammetry (CV), scanned at 0.2 mV/s and cycled between 0.005 and 3.0 V *vs.* Li^+/Li (Figure 3a). CV curve shows the similar redox peaks for Sn reaction with Li^+ to $Li_{4.4}Sn$ at 1.65 and 0.85 V and extraction of lithium occurred at 0.27 V and 2.1 V during cathodic and anodic sweep, respectively. The peak appear near 0.5 V during cathodic scan corresponds to the breakdown of electrolyte to form SEI film but no peak observed in the successive cycles that confirm high reversibility and control over SEI layer thickness [10]. Furthermore, a small peak appears at 1.35 V confirms the synergism among the $CoSn_x$ core and N-PGC matrix [11]. It is worth noting that no peak was observed during anodic scan for Co which demonstrates its completely inactive nature [41]. Moreover, to confirm the high rate capability of hybrid, CV scans at different rates were carried out, as shown in Figure S15. It is worth noting that similar profile of CV curves at different scan rates were obtained, which assures high rate capability of the hybrid and easy access of redox sites due to unique internal structure. In contrast to hybrid electrode, the electrode of Sn shows huge difference among first and successive cycles that confirm the formation of very thick SEI layer on the surface of electrode and further reduction of current intensity in successive cycles confirm the reformation of SEI (Figure S16) because raptured surface exposed fresh surface of tin that increases SEI film thickness *via* irreversible storage of Li^+. The voltage profiles of hybrid (Figure 3b) exhibited typical electrochemical features of CoSn (here broader voltage range of 5 mV to 3 V was used for the complete exploration of stability of electrode developed with unique composition but the redox reaction is in the limits of anode cut of voltage) [12,42], with almost no change over 100 cycles. Further,

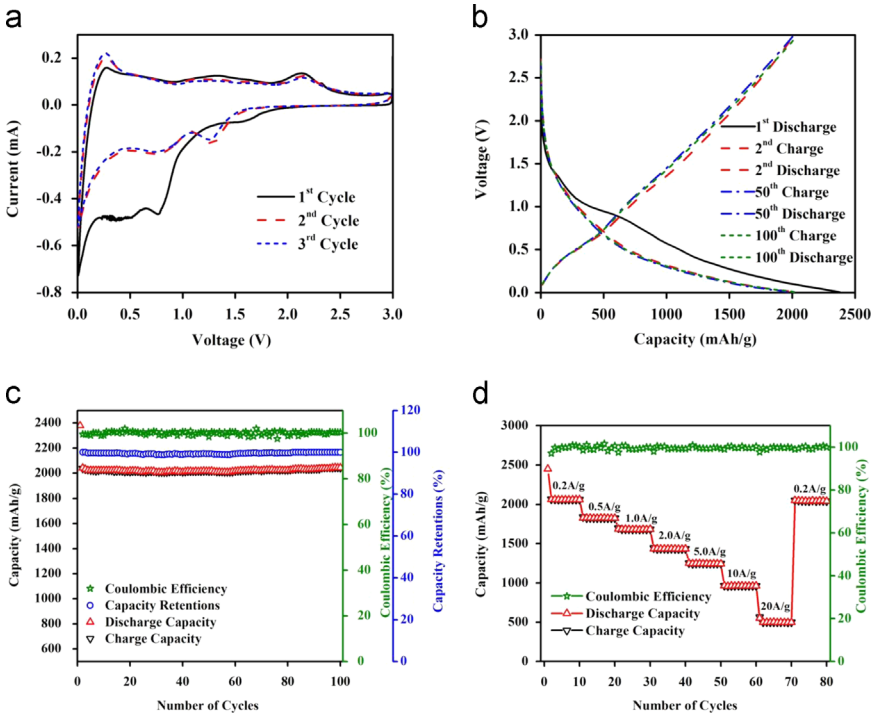

Figure 3 (a) Cyclic voltammograms of $CoSn_x$@C-PAn at scan rate of 0.2 mV/s in the voltage range of 0.005-3 V *vs.* Li^+/Li. (b) Galvanostatic charge-discharge curves of $CoSn_x$@C-PAn hybrid cycled 1st, 2nd, 50th and 100th tested at current density of 0.2 A/g in the range of 0.005-3 V *vs.* Li^+/Li. (c) Cyclic performance, capacity retention and Coulombic efficiency of $CoSn_x$@C-PAn for 100 cycles at current density of 0.2 A/g in the voltage range of 0.005-3 V *vs.* Li^+/Li. (d) The cyclic performance and Coulombic efficiency of $CoSn_x$@C-PAn at different current densities in the voltage range of 0.005-3 V *vs.* Li^+/Li.

absence of large plateaus confirms the faster transfer of lithium inside the electrode through porous carbon and grain boundaries as proved by HRTEM studies (Figure 2c-e) [43,44], in contrast to the electrode that shows large irreversible storage of lithium in the first cycle and in successive cycles required large time to diffuse, resulting poor CR_t (Figure S17). [45] Furthermore, it is point of ponder that faster diffusion of Li^+ is necessary for high rate capability and the linear profile is indication of faster diffusion through shorter distance (below 10 nm) [46]. In fact, the grain boundaries serve as tunnels inside the NPs for faster transfer of Li^+ and Co provides faster electron flow to redox sites as results an efficient redox reaction happened in a short time, thus result in linear charge-discharge profile with improved performance as discussed by Gogotsi and Okubo et al. [43,46]. The CE is an indicator of the reversibility of the electrochemical reaction at electrode [14]. The decrease in CE usually happens due to rupture and reformation of SEI layer, especially in later cycles. After initial few cycles, CE remains nearly 100% during charging and discharging process of the hybrid electrode (Figure 3c and d). It should be noted that low areal mass loadings were frequently used to achieve the stable cycling life. However, high mass loadings are needed to realize the high performance for electrification of road market [14]. The hybrid shows first discharge capacity of 2379.4 mAh/g with mass loading of 3.8 g/cm^2 (further the tap density of the as-synthesized hybrid is 0.46 g/cm^3 and this is in the desirable range for electrode material as Sn based materials show large volume changes) at current density of 0.2 A/g and capacity retention was as high as 100% (calculated from 2nd discharge) after 100 cycles. While the hybrid shows 85.64% de-lithiation of its first lithiation process and result in capacity of 2037.8 mAh/g. The loss of 341.6 mAh/g capacity is because of the SEI film formation that was overcame in the next cycles with improved CE. Furthermore, the plateaus in the first discharge curve well concise with CV curve and show two major changes first the lithium storage through the conversion reaction with Sn; second through insertion in the carbon matrix as indicated by the plateau below 0.5 V that continues till the cut off voltage reaches. Further to explore the practical utilization of as-developed hybrid, its electrochemical performances were explored in various voltage widows (0.005 to 1.5 and 0.005 to 0.6 V) as for practical utilizations the upper voltage limit of anode should be restricted below 1.2-1.3 V [12]. It is worth noting that hybrid outperformed even in the restricted voltage windows and shows the discharge capacities of 1524.76 and 880.12 mAh/g after 100 cycles with CR_t of ~99% at current density of 0.2 A/g in the voltage range of 0.005-1.5 V and 0.005-0.6 V, respectively as shown in Figure S18. In addition the CE values reach to 100% after initial few cycles that further emphasized the high reversibility of the hybrid in the restricted voltage windows. The stable CE and high CR_t demonstrated that hybrid is highly feasible for deep diffusion of Li^+ and all material is active in thick electrode. To observe the effect of mass loading on the performance of hybrid 4 electrodes were assembled with different mass loadings (2-4 mg/cm^2) and it was found that increasing mass loading has minimal effect on performance (Figure S19). Furthermore, similar performance shows high repeatability of the results and further exclude the influence of other factors likewise cell assembly, testing conditions *etc.* Stable structure at particle level is highly required to achieve

stable long cycling of a high mass loaded electrode, because electrode level cracking and failure can be possible even with small changes in particle morphology which accumulate across the thickness of electrode. A successful design of the hybrid structure is indicated by stable and excellent performance at high mass loading. To explore the rate capability, hybrid was tested at various current densities and it is found that hybrid keeps its reversibility with changing current densities as shown by stable CE (Figure 3d). The hybrid keeps its reversible capacity as high as 551 mAh/g at higher current density of 20 A/g and restores its excellent performance of 2040.5 mAh/g with decrease in current density to 0.2 A/g (Figure 3d). Thus, high rate capability along with higher performance proves the reliability of the developed method to control over large volume changes of anode materials.

Furthermore, hybrid was tested for 1000 cycles at 10 A/g to evaluate the long cyclic life of electrode. It is found that hybrid keeps a capacity of 956.4 mAh/g after 1000th cycle with high CR_t of 98.5% (only 0.0015% capacity loss per cycle) and stable CE around 100% (Figure 4a). The stability of structure after electrochemical test was examined through TEM and HRTEM after washing electrode material with acid to remove SEI layer (Figure S20). From microscopic analysis, it is evaluated that the structure (measured *d*-spacing of 0.199 nm corresponds to (310) plane of $CoSn_2$ (JCPDS no. 25-0256)) and size of NPs in hybrid are preserved after long cycling test. Moreover, the stability concern of hybrid was examined by electrochemical impedance spectroscopy (EIS) before and after 1000 cycles (Figure 4b). Similar Nyquist profile was obtained for hybrid before and after 1000 cycles as both curves show semicircle in high frequency region and a straight vertical inclined line in lower frequency. The SEI layer impedance (R_f) and charge transfer resistance (R_{ct}) were measured using appropriate Randles equivalent circuit shown in Figure S21a [5]. The calculated R_f and R_{ct} before testing is 16.39 Ω and 72.14 Ω that slightly increased to 18.53 Ω and 75.14 Ω after 1000 cycles of testing, respectively. Vertical spikes confirmed the capacitive behavior of hybrid but a little increment in ions diffusion resistance (Warburg impedance, *W*) was observed after long cyclic life. Better electron/ion conductivity over prolonged cycles with strong resistance control for successive charge–discharge cycles suggest extraordinary CR_t, CE and high stability of hybrid. To the best of our knowledge, long stable life with excellent performance at such high mass loadings is rarely reported for Sn-based electrodes.

Synergistic effect of Co doping, C coating and N-PGC with Sn was analyzed by comparative electrochemical studies of PAn, Sn, Sn@C, Co_2SnO_4, Co_2SnO_4–PAn, $CoSn_x$ and $CoSn_x$@C–PAn. It is simply perceived from Figure 4c that after making hybrids of two structures the performance increased, which indicated that materials took successfully the advantages of both components for better performance due to strong interfacial interactions. The performance of Sn@C is increased after carbon coating but still a large capacity loss was observed in the initial cycles. The fact that increasing the electronic conductivity of Sn *via* carbon coating can improve the performance through faster Li^+ diffusion, but lithium intercalation reaction ($Li_{4.4}Sn$) may be limited by electron transfer between the carbon coating and redox site in the crystal [47]. It is noticeable that when the intrinsic conductivity of Sn was increased through Co doping, an improved performance was achieved but capacity loss at initial cycles still exist because of surface reactions. Thus, by combining Co doping and constructing shell of carbon in one structure ($CoSn_x$@C–PAn), an extraordinary reversible

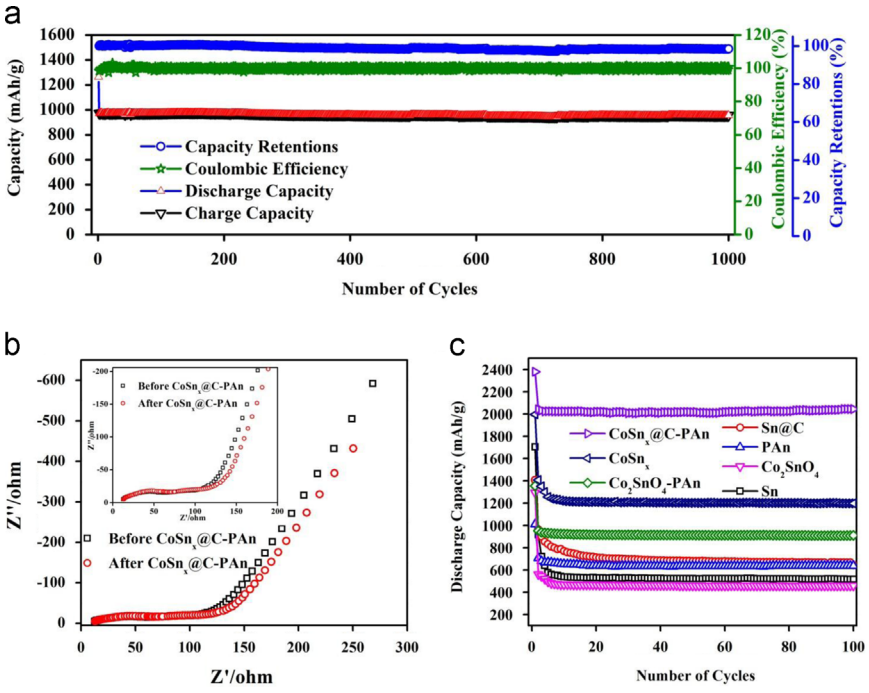

Figure 4 (a) Cyclic performance, capacity retention and Coulombic efficiency of $CoSn_x$@C–PAn for 1000 cycles at current density of 10 A/g in the voltage range of 0.005–3 V *vs.* Li^+/Li. (b) Nyquist plots of $CoSn_x$@C–PAn hybrid before and after 1000 cycles of charge–discharge in the range of 100 kHz to 10 mHz at open circuit potential (the inset is Nyquist plot with equal *x*-*y* axis ratio at high resolution). (c) Comparison of discharge capacities of $CoSn_x$@C–PAn, $CoSn_x$, Co_2SnO_4–PAn, Co_2SnO_4, Sn@C, Sn and PAn at current density of 0.2 A/g in the voltage range of 0.005–3 V *vs.* Li^+/Li.

performance is attained with high CR_t. Further the incorporation of hard Co also prevents the rapture of C shell around the NPs by compensating the internal stresses as over expansion of NPs causes the rapturing of the C shell [48]. It is worth noting that carbon matrix with well-defined pore size (1–1.5 nm) provide highway to both electrons and ions through pore walls and pores, respectively. These pores provide tunnels for deep and fast diffusion of Li^+ in thick electrode to keep the entire material active, which is further facilitated by the internal grain boundaries of NPs to achieve faster redox reaction by shortening the internal diffusion path. The relative sizes of Li^+ ions and pores of the electrode materials are also very important in determining the potential performance. In our designed system, Li^+ (0.076 nm) can easily diffuse through the electrode materials (pore size 1.5 nm) not only providing higher performance but also higher rate capability [49,50]. In addition, higher capacity is observed than the theoretical capacity of Sn, this additional capacity comes up from the interfacial storage of Li^+ due the existence of mixed phase by space layer charge that is energetically favorable at interface of two phases as shown in Scheme 1, intercalation of Li^+ in N-PGC through conversion reaction of Li_x/C_6 that contributes large capacity and synergistic effect between NPs and N-PGC [31,33,35]. The existence of nitrogen in the carbon make it more electrochemical active that results higher performance (Figure 4c) and contribute lager capacity to hybrid performance. As, nitrogen is capable to change the electronic structure and density of state to improve the conductivity and capacity of graphitic carbon [24]. To further explore the synergism of different components, EIS studies were done and representative Nyquist plots are shown in Figure S21b. In the light of above results, the optimized cycling stability and rate capability of hybrid is attributed to the enhanced transport kinetics and structural stability. The high transport kinetics comes from N-PGC conductive network that provides faster electronic highway from current collector to active material and among the separated NPs as well as Co improves the intrinsic transfer of electron from carbon to redox sites which make available all the material for higher performance. The homogenously porous structure and anisotropic adhesion realizes efficient mass transfer of Li^+. Furthermore, the structure is protected *via* accommodating internal strains by hard Co, preventing surface reactions by carbon shell and presence of adaptable matrix of N-PGC.

Conclusions

In summary, $CoSn_x$@C–PAn hybrid has been fabricated utilizing low-cost and large scale aqueous chemical growth under industrially acceptable conditions to control large volume changes and make accessible all active sites of Sn-based anode *via* active–inactive metal phase embedded in N-PGC matrix. The hybrid efficiently took the advantages of mixed phase, enhanced internal conductivity by hard Co doping, surface protection by carbon shell and high surface area (438.5 m^2/g) with well-defined pore size (1–1.5 nm) to improve the transport kinetics, lithium intercalation reaction (Li_6/C_6) in fused C_6 aromatic ring of N-PGC and structural stability. The hybrid possess high capacity of 2044 mAh/g with extraordinary CE and CR_t of ~100% after 100 cycles at 0.2 A/g with the mass loading of 3.8 mg/cm^2. Furthermore, hybrid shows long cyclic stability for 1000 cycles of charge–discharge at current density of 10 A/g with capacity of 1256 mAh/g after 1000th cycle and impedance calculations confirm slight change in resistances after 1000 cycles. The rate capability of the hybrid is explored by testing at different current densities and hybrid keeps 551 mAh/g even at 20 A/g. The approach to build active–inactive metal phase encapsulated in carbon shell and embedded in N-PGC adaptable matrix established here opens up a new avenue to control volume changes and brings high performance of tin-based anode, can also be extended to other attractive anode (like Silicon, Germanium, *etc.*) and cathode materials systems that suffer large structural changes during conversion reactions.

Supporting information

Supporting Information is available from the Elsevier or the author [part of experimental section, XRD of PAn before and after annealing, Raman and FTIR results of hybrid, XRD of Sn NPs, STEM image of hybrid, TEM images of hybrid, Co_2SnO_4 NPs, PAn before and after annealing, hybrid at different temperature, high resolution spectra of Sn3d and Co2p, Sn and Sn@C NPs, Hybrid after testing, SAED of hybrid and Sn NPs, HRTEM, of hybrid after testing, NPs distribution graph, PAn polymerization reaction mechanism, CV of Sn NPs, capacity performance of hybrid at different mass loading, behavior of bulk and nanomaterials towards Li^+ storage, Nyquist plot and equivalent circuit diagram].

Acknowledgments

This work was supported by the NSFC-RGC Joint Research Scheme (51361165201), NSFC (51125001 and 51172005), Beijing Natural Science Foundation (2122022), Aerostatic Science Foundation (2010ZF71003) and Doctoral Program of the Ministry of Education of China (20120001110078).

Appendix A. Supporting information

Supplementary data associated with this article can be found in the online version at http://dx.doi.org/10.1016/j.nanoen.2015.05.035.

References

[1] C. Zhang, N. Mahmood, H. Yin, F. Liu, Y. Hou, Adv. Mater. 25 (2013) 4932.
[2] Y. Idota, T. Kubota, A. Matsufuji, Y. Maekawa, T. Miyasaka, Science 276 (1997) 1395–1397.
[3] P. Poizot, S. Laruelle, S. Grugeon, L. Dupont, J.M. Tarascon, Nature 407 (2000) 496–499.
[4] J. Jiang, Y. Feng, N. Mahmood, F. Liu, Y. Hou, Sci. Adv. Mater. 5 (2013) 1667–1675.
[5] N. Mahmood, C. Zhang, Y. Hou, Small 9 (2013) 1321–1328.
[6] N. Mahmood, C. Zhang, J. Jiang, F. Liu, Y. Hou, Chemistry 19 (2013) 5183–5190.
[7] R.N. Nasim Khan, N. Mahmood, C. Lv, G. Sima, J. Zhang, J. Hao, Y. Hou, Y. Wei, RSC Adv. 4 (2014) 7374–7379.
[8] J. Shin, W.-H. Ryu, K.-S. Park, I.-D. Kim, ACS. Nano 7 (2013) 7330–7341.

[9] B. Luo, B. Wang, X. Li, Y. Jia, M. Liang, L. Zhi, Adv. Mater. 24 (2012) 3538–3543.
[10] N. Mahmood, C. Zhang, F. Liu, J. Zhu, Y. Hou, ACS Nano 7 (2013) 10307–10318.
[11] B. Luo, B. Wang, M. Liang, J. Ning, X. Li, L. Zhi, Adv. Mater. 24 (2012) 1405–1409.
[12] Y. Zou, Y. Wang, ACS Nano 5 (2011) 8108–8114.
[13] Y. Yang, X. Fan, G. Casillas, Z. Peng, G. Ruan, G. Wang, M. J. Yacaman, J.M. Tour, ACS Nano 8 (2014) 3939–3946.
[14] N. Liu, Z. Lu, J. Zhao, M.T. McDowell, H.-W. Lee, W. Zhao, Y. Cui, Nat. Nanotechnol. 9 (2014) 187–192.
[15] P. Chen, L. Guo, Y. Wang, J. Power Sources 222 (2013) 526–532.
[16] J. Deng, H. Ji, C. Yan, J. Zhang, W. Si, S. Baunack, S. Oswald, Y. Mei, O.G. Schmidt, Angew. Chem. Int. Ed. 52 (2013) 2326–2330.
[17] C. Zhai, N. Du, H. Zhang, J. Yu, P. Wu, C. Xiao, D. Yang, Nanoscale 3 (2011) 1798.
[18] N. Zhang, Q. Zhao, X. Han, J. Yang, J. Chen, Nanoscale 6 (2014) 2827–2832.
[19] J. Luo, J. Liu, Z. Zeng, C.F. Ng, L. Ma, H. Zhang, J. Lin, Z. Shen, H.J. Fan, Nano Lett. 13 (2013) 6136–6143.
[20] K.T. Lee, S. Jeong, J. Cho, Acc. Chem. Res. 46 (2012) 1161–1170.
[21] W. Lu-e, R. Xu-mei, W. Feng, Adv. Mater. Res. 391–392 (2011) 23–3636.
[22] H. Lee, M. Yanilmaz, O. Toprakci, K. Fu, X. Zhang, Energy Environ. Sci. 7 (2014) 3857–3886.
[23] S.M. Hwang, Y.-G. Lim, J.-G. Kim, Y.-U. Heo, J.H. Lim, Y. Yamauchi, M.-S. Park, Y.-J. Kim, S.X. Dou, J.H. Kim, Nano Energy 10 (2014) 53–62.
[24] N. Mahmood, C. Zhang, H. Yin, Y. Hou, J. Mater. Chem. A 2 (2014) 15.
[25] C. Nan, Z. Lin, H. Liao, M.K. Song, Y. Li, E.J. Cairns, J. Am. Chem. Soc. 136 (2014) 4659–4663.
[26] M.-Y. Li, C.-L. Liu, M.-R. Shi, W.-S. Dong, Electrochim. Acta 56 (2011) 3023–3028.
[27] B. Wang, H.B. Wu, L. Zhang, X.W. Lou, Angew. Chem. Int. Ed. 52 (2013) 4165–4168.
[28] W. Xu, J. Wang, F. Ding, X. Chen, E. Nasybulin, Y. Zhang, J.-G. Zhang, Energy Environ., Sci 7 (2014) 513.
[29] J. Xiao, X. Wang, X.-Q. Yang, S. Xun, G. Liu, P.K. Koech, J. Liu, J.P. Lemmon, Adv. Funct. Mater. 21 (2011) 2840–2846.
[30] X. Lai, J.E. Halpert, D. Wang, Energy Environ. Sci. 5 (2012) 5604.
[31] X. Han, G. Qing, J. Sun, T. Sun, Angew. Chem. Int. Ed. 51 (2012) 5147–5151.
[32] Y.J. Mai, J.P. Tu, C.D. Gu, X.L. Wang, J. Power Sources 209 (2012) 1–6.
[33] P. Zhang, L. Wang, J. Xie, L. Su, C.-a. Ma, J. Mater. Chem. A 2 (2014) 3776.
[34] Y.M. Jiang, K.X. Wang, H.J. Zhang, J.F. Wang, J.S. Chen, Sci. Rep. 3 (2013) 3490.
[35] Y.-Y. Hu, Z. Liu, K.-W. Nam, O.J. Borkiewicz, J. Cheng, X. Hua, M. T. Dunstan, X. Yu, K.M. Wiaderek, L.-S. Du, K.W. Chapman, P. J. Chupas, X.-Q. Yang, C.P. Grey, Nat. Mater. 12 (2013) 1130–1136.
[36] C. Zhang, R. Hao, H. Yin, F. Liu, Y. Hou, Nanoscale 4 (2012) 7326–7329.
[37] C. Zhang, R. Hao, H. Liao, Y. Hou, Nano Energy 2 (2013) 88–97.
[38] A. Vu, Y. Qian, A. Stein, Adv, Energy Mater. 2 (2012) 1056–1085.
[39] X. Liang, M. Zhang, M.R. Kaiser, X. Gao, K. Konstantinov, R. Tandiono, Z. Wang, H.-K. Liu, S.-X. Dou, J. Wang, Nano Energy 11 (2015) 587–599.
[40] I. Sapurina, J. Stejskal, Polym. Int. 57 (2008) 1295–1325.
[41] G. Ferrara, C. Arbizzani, L. Damen, M. Guidotti, M. Lazzari, F. G. Vergottini, R. Inguanta, S. Piazza, C. Sunseri, M. Mastragostino, J. Power Sources 211 (2012) 103–107.
[42] Y. Xu, Q. Liu, Y. Zhu, Y. Liu, A. Langrock, M.R. Zachariah, C. Wang, Nano Lett. 13 (2013) 470–474.
[43] P. Simon, Y. Gogotsi, B. Dunn, Science 343 (2014) 1210–1211.
[44] X. Liu, J. Zhang, W. Si, L. Xi, S. Oswald, C. Yan, O.G. Schmidt, Nanoscale 7 (2015) 282–288.
[45] W.-M. Zhang, J.-S. Hu, Y.-G. Guo, S.-F. Zheng, L.-S. Zhong, W.-G. Song, L.-J. Wan, Adv. Mater. 20 (2008) 1160–1165.
[46] M. Okubo, E. Hosono, J. Kim, M. Enomoto, N. Kojima, T. Kudo, H. Zhou, I. Honma, J. Am. Chem. Soc. 129 (2007) 7444–7452.
[47] P. Bai, M.Z. Bazant, Nat. Commun. 5 (2014) 3585.
[48] X.H. Liu, J.Y. Huang, Energy Environ. Sci. 4 (2011) 3844–3860.
[49] J. Chmiola, C. Largeot, P.L. Taberna, P. Simon, Y. Gogotsi, Angew. Chem. Int. Ed. 47 (2008) 3392–3395.
[50] C. Largeot, C. Portet, J. Chmiola, P.-L. Taberna, Y. Gogotsi, P. Simon, J. Am. Chem. Soc. 130 (2008) 2730–2731.

Nasir Mahmood obtained his BS degree in 2009 in Chemistry from Punjab University and MS degree in 2011 in Materials and Surface Engineering from National University of Science and Technology, Pakistan. He joined Peking University in 2011, where he is currently pursuing his Ph.D in Materials Science and Engineering under the guidance of Prof. Yanglong Hou. His research involves the synthesis of graphene/graphene-based nanomaterials and their application in energy storage and conversion devices.

Jinghan Zhu received her B.S. in Materials Science and Engineering from the University of Science and Technology Beijing (USTB, China) in 2011. She has been pursuing her Ph.D under the supervision of Prof. Yanglong Hou in the Department of Materials Science and Engineering at Peking University since 2011. Her research interests are the chemical synthesis of graphene based nanomaterials and their magnetic and catalytic applications.

Sarish Rehman obtained his BS degree in Chemistry from Peshawar University in 2010 and her MS degree in 2013 in Materials and Surface Engineering from the National University of Science and Technology, Pakistan. She joined Peking University in 2013, where she is currently pursuing her Ph.D in Materials Science and Engineering. Her research focuses on the synthesis and development of novel nanomaterials for the application in energy storage and conversion devices.

Quan Li received her Ph.D in Materials Science and Engineering from Northwestern University in 2001. She joined The Chinese University of Hong Kong as an assistant professor in 2002, and was promoted to full professor in 2011. Her research focuses on functional materials, including the fabrication and assembly of nanomaterials, characterizations and measurements of individual nanostructures, and their applications in energy and biomedicine.

Yanglong Hou received his Ph.D in Materials Science from Harbin Institute of Technology (China) in 2000. After a short post-doctoral training at Peking University, he worked at the University of Tokyo from 2002 to 2005 as JSPS foreign special researcher and also at Brown University from 2005 to 2007 as postdoctoral researcher. He joined Peking University in 2007, and now is a Chang Jiang Chair Professor of Materials Science. His research interests include the design and chemical synthesis of functional nanoparticles and graphene, and their biomedical and energy related applications.